

**Hydrogen Production from Water by Photosynthesis
System I for Use as Fuel in Energy Conversion Devices
(a.k.a. Understanding Photosystem I as a Biomolecular
Reactor for Energy Conversion)**

**by Cynthia A. Lundgren, David Baker, Barry Bruce, Maggie Hurley,
Amy K. Manocchi, Scott Pendley, and James Sumner**

ARL-TR-6904

April 2014

NOTICES

Disclaimers

The findings in this report are not to be construed as an official Department of the Army position unless so designated by other authorized documents.

Citation of manufacturer's or trade names does not constitute an official endorsement or approval of the use thereof.

Destroy this report when it is no longer needed. Do not return it to the originator.

Army Research Laboratory

Adelphi, MD 20783-1197

ARL-TR-6904**April 2014**

Hydrogen Production from Water by Photosynthesis System I for Use as Fuel in Energy Conversion Devices (a.k.a. Understanding Photosystem I as a Biomolecular Reactor for Energy Conversion)

Cynthia A. Lundgren, David Baker, Amy K. Manocchi, and James Sumner
Sensors and Electron Devices Directorate, ARL

Maggie Hurley and Scott Pendley
Weapons and Materials Research Directorate, ARL

Barry Bruce
University of Tennessee-Knoxville

REPORT DOCUMENTATION PAGE				Form Approved OMB No. 0704-0188	
<p>Public reporting burden for this collection of information is estimated to average 1 hour per response, including the time for reviewing instructions, searching existing data sources, gathering and maintaining the data needed, and completing and reviewing the collection information. Send comments regarding this burden estimate or any other aspect of this collection of information, including suggestions for reducing the burden, to Department of Defense, Washington Headquarters Services, Directorate for Information Operations and Reports (0704-0188), 1215 Jefferson Davis Highway, Suite 1204, Arlington, VA 22202-4302. Respondents should be aware that notwithstanding any other provision of law, no person shall be subject to any penalty for failing to comply with a collection of information if it does not display a currently valid OMB control number.</p> <p>PLEASE DO NOT RETURN YOUR FORM TO THE ABOVE ADDRESS.</p>					
1. REPORT DATE (DD-MM-YYYY) April 2014		2. REPORT TYPE DSI-Final		3. DATES COVERED (From - To) 10/1/2010-10/1/2013	
4. TITLE AND SUBTITLE Hydrogen Production from Water by Photosynthesis System I for Use as Fuel in Energy Conversion Devices (a.k.a. Understanding Photosystem I as a Biomolecular Reactor for Energy Conversion)				5a. CONTRACT NUMBER	
				5b. GRANT NUMBER	
				5c. PROGRAM ELEMENT NUMBER	
6. AUTHOR(S) Cynthia A. Lundgren, David Baker, Barry Bruce,* Maggie Hurley, Amy K. Manocchi, Scott Pendley, and James Sumner				5d. PROJECT NUMBER	
				5e. TASK NUMBER	
				5f. WORK UNIT NUMBER	
7. PERFORMING ORGANIZATION NAME(S) AND ADDRESS(ES) U.S. Army Research Laboratory ATTN: RDRL-SED-C 2800 Powder Mill Road Adelphi, MD 20783-1197				8. PERFORMING ORGANIZATION REPORT NUMBER ARL-TR-6904	
9. SPONSORING/MONITORING AGENCY NAME(S) AND ADDRESS(ES)				10. SPONSOR/MONITOR'S ACRONYM(S)	
				11. SPONSOR/MONITOR'S REPORT NUMBER(S)	
12. DISTRIBUTION/AVAILABILITY STATEMENT Approved for public release; distribution unlimited.					
13. SUPPLEMENTARY NOTES *University of Tennessee-Knoxville, Knoxville, TN 37996					
14. ABSTRACT In this program we have developed a solid-state device with an immobilized Photo System I (PSI) to generate H ₂ from H ₂ O. We used a three-prong approach, which includes: (1) genetic engineering of PSI to remove or modify specific regions to enable coupling of the PSI active site and electrode surface and improve electron transfer to PSI through modifications to cytochrome, and increase PSI packing and minimize dead space on surfaces by monomerizing PSI; (2) self- or assisted-assembly of PSI onto various engineered electrode surfaces using self-assembled monolayers (SAMs) and redox polymers and their photo-/electrochemistry; and (3) computational analysis of PSI and proposed modifications to optimize surface binding and electron transfer. The computational approach incorporates coarse- and fine-grained docking to study protein-protein and protein-surface interactions; coarse-grained (CG) molecular dynamics (MD) for extended studies of the PSI complex; all atom (AA) molecular dynamics to study thermal relaxation of the PSI complex and protein-protein interactions; and quantum mechanics (QM) to study electron transport phenomenon.					
15. SUBJECT TERMS Photo System I, hydrogen evolution, modified electrodes					
16. SECURITY CLASSIFICATION OF:			17. LIMITATION OF ABSTRACT UU	18. NUMBER OF PAGES 37	19a. NAME OF RESPONSIBLE PERSON Cynthia A. Lundgren
a. REPORT Unclassified	b. ABSTRACT Unclassified	c. THIS PAGE Unclassified			19b. TELEPHONE NUMBER (Include area code) 301-394-2541

Contents

List of Figures	v
List of Tables	vi
Acknowledgments	vii
1. Objective	1
2. Approach	1
2.1 Biochemical Approach.....	1
2.1.1 Protein Engineering for Enhanced Electron Donation to PSI	1
2.1.2 Conversion of the PSI Trimer Into a Functional Monomer	2
2.2 Abiotic Integration Approach, Materials, and Methods.....	3
2.2.1 Surface Assembly	3
2.2.2 Electrochemical and Photoelectrochemical Approach.....	4
2.3 Multiscale Modeling Approach.....	5
2.3.1 PSI Surface Interactions and Environmental Effects	5
2.3.2 PSI – cyt c ₆ Complex Structure and Interactions	5
2.3.3 Molecular Dynamics Approaches	5
2.3.4 Force Field Parameterization.....	6
2.3.5 Quantum Mechanics	6
3. Results	7
3.1 Biochemical Approach.....	7
3.1.1 Conversion of the PSI Trimer Into a Functional Monomer	7
3.2 Abiotic Integration Approach (Electrochemistry and Photoelectrochemistry).....	10
3.2.1 PSI Surface Assembly	10
3.2.2 Polymer Hosts and Encapsulation.....	11
3.2.3 Pt Catalysts	13
3.3 Multiscale Modeling Results.....	14
3.3.1 PSI Surface Interactions and Environmental Effects	14
3.3.2 PSI – cyt c ₆ Complex Structure.....	16
3.3.3 Molecular Dynamics	16
3.3.4 Quantum Mechanics.....	18

4. Conclusions	20
5. References	21
6. Transitions	23
List of Symbols, Abbreviations, and Acronyms	25
Distribution List	27

List of Figures

Figure 1. Schematic of the photosynthetic pathway in microorganisms. This project is focused on PSI and its role with cytochrome, plastocyanin, ferredoxin, and their synthetic (abiotic) replacements.	2
Figure 2. Improved surface coverage using electrodeposited trimers and monomers.....	3
Figure 3. PSI monomer preparation from PSI trimer	8
Figure 4. Transient absorption of monomer and trimer PSI with various flash times (a) and different flash intensities (b). The monomer and trimer were fit to determine the Hill coefficients.....	9
Figure 5. Photocurrent response of monomer (a) and trimer (b) electrodes at various incident light powers, wavelength 676 nm.	9
Figure 6. Summation of the results from immobilization of PSI on self-assembled monolayers of modified alkane thiols on gold substrates.....	11
Figure 7. Absorbance spectrum (A) of PSI trimer solution. IPCE photoaction spectra (B) of PSI monomer (a) and trimer (b).....	12
Figure 8. Optimization of PSI in the Nafion films. The current output reaches a maximum at $100\mu\text{g}/\text{cm}^2$. The turnover rate shows that the current from an individual protein is reduced due to blocking effects from upper layers.....	13
Figure 9. Pt nanoparticles capped with mercaptohexanoic acid. The nanoparticles were dropcast onto the TEM grid and air dried. Reduction was performed by NaBH_4 . The scale bar is 10 nm.....	14
Figure 10. (a) Representation of the hydrophobicity (blue represents hydrophilic, red represents hydrophobic); and (b) residue character (red represents acidic, blue represents basic, white represents nonpolar, and green represents polar residues) of the PSI luminal surface.....	15
Figure 11. (Left) Relaxed structure (silver) of the PSI complex after molecular dynamics, compared to the original crystal structure (red). (Right) the unfolding in the stromal hump is seen in the growth of Root Mean Square Deviation (RMSD) from the crystal structure coordinates during the course of the simulation	17
Figure 12. Molecular dynamics simulation with the improved iron-sulfur center parameters showing greatly improved stability.....	17

List of Tables

Table 1. Predicted distance (Angstroms) between heme iron atoms.	16
Table 2. Measured distances between electron carriers in the PSI x-ray and initial MD structures	18
Table 3. Physical and electronic structure properties of three P700 models at B3LYP/6-31G (d, p).....	19

Acknowledgments

The authors would like to extend thanks to the following individuals for all of the contributions they have made to the project:

Mr. Richard Simmerman, Mr. Khoa Nguyen, and Mr. Meng Li, graduate students of Prof. Barry D. Bruce at the University of Tennessee-Knoxville, who have provided Photo System I (PSI) material and insight into the proteins. Mrs. Melissa Lamicq and Mr. Jordan Bryner for their participations as summer undergraduate researchers at the U.S. Army Research Laboratory (ARL).

INTENTIONALLY LEFT BLANK.

1. Objective

The ever-increasing world energy demand, coupled with heightened concerns of global warming, has generated considerable interest in alternative energy sources. Countless research groups have focused on developing hydrogen fuel cells as an alternative energy source; however, the on-demand production of clean hydrogen fuel remains challenging. Nature has perfected the conversion of light energy to chemical energy via photosynthesis through a finely tuned network of protein reaction centers. Photo System I (PSI), a thylakoid reaction center protein, is particularly instrumental in photosynthesis. Our goal is to mimic photosynthesis through the fabrication of a photocatalytic biohybrid system of PSI and inorganic materials to produce hydrogen gas. This process is accomplished through a three-pronged approach: (1) modification of PSI to improve packing on and coupling to the electrode surface and improve electron transfer efficiency; (2) developing chemical and electrochemical techniques to design, analyze, and improve the electrode surfaces with hard wiring of mediators and their photoelectrochemistry; and (3) computationally analyzing the resulting protein complex and surface interactions to optimize surface binding and electron transfer.

2. Approach

2.1 Biochemical Approach

2.1.1 Protein Engineering for Enhanced Electron Donation to PSI

In a light-driven process, PSI transfers electrons from soluble cytochrome c_6 (cyt- c_6) or plastocyanin (PC) in the lumen (intracellular) to soluble ferredoxin (Fd) in the stroma (extracellular) as pictured in figure 1 (1). The rate of this charge-separation process is limited by binding of the soluble donor and acceptor proteins to PSI. Cyt- c_6 is a soluble electron carrier found in photosynthetic prokaryotes (2). Cyt- c_6 docks with PSI near a portion of the protein called PsaF and donates electrons to the special pair of the redox active reaction site, P700, which then undergoes a photoinduced charge separation and allows the excited electron to move across PSI via a series of electron acceptors (3). It is hypothesized that the binding of cyt- c_6 is the rate-limiting step in electron transfer from the cytochrome to PSI in prokaryotes (4). It seems reasonable to assume this would also be the case in the cyanobacteria used in this study.

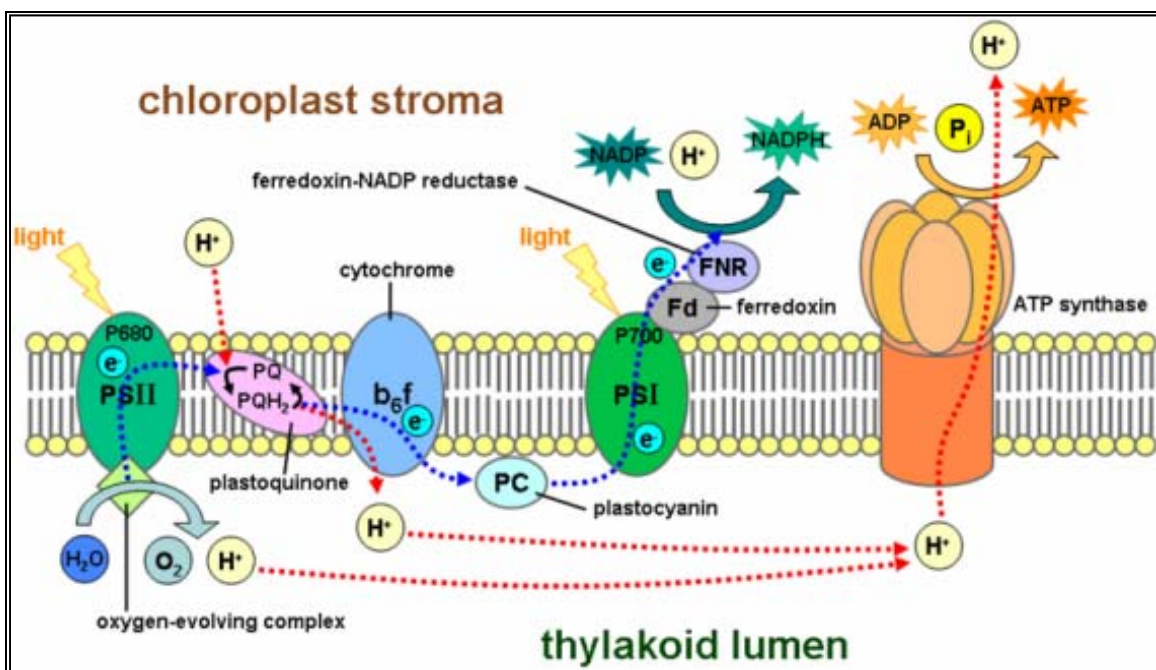


Figure 1. Schematic of the photosynthetic pathway in microorganisms. This project is focused on PSI and its role with cytochrome, plastocyanin, ferredoxin, and their synthetic (abiotic) replacements.

One goal is to increase binding affinity between cyt- c_6 and PSI from *Thermosynechococcus elongatus* (*T.e.*) by engineering chains of cyt c_6 containing multiple (up to five) cyt c_6 's. The expected increase in binding affinity should improve electron transport rates in the photosystem. This was planned to take the advantage of the slow off-rate seen in eukaryotic cyt- c_6 by allowing all of the cytochromes to be reduced and sequentially transferring electrons to P700. The linked cytochromes can potentially be re-reduced in the PSI bound state because of the extended luminal exposure, resulting in a continuous electron transfer to P700.

2.1.2 Conversion of the PSI Trimer Into a Functional Monomer

PSI has been utilized for hydrogen production and photovoltaic applications. In the membranes of cyanobacteria, this complex exists as a trimeric complex with a three-fold axis of symmetry, as seen in figure 2. However, each monomer is capable of individual light-driven charge separation and can reduce Fd *in vivo* and *in vitro*. This trimeric structure is very large, with a molecular weight >1 MDa (5). This large size complicates efforts to develop an efficient process of assembly on surfaces and may also lead to rate limitations of electron transfer. One solution to this packing problem of the large PSI trimer is to also have the smaller monomeric complex available to “fill” in between the larger complexes.

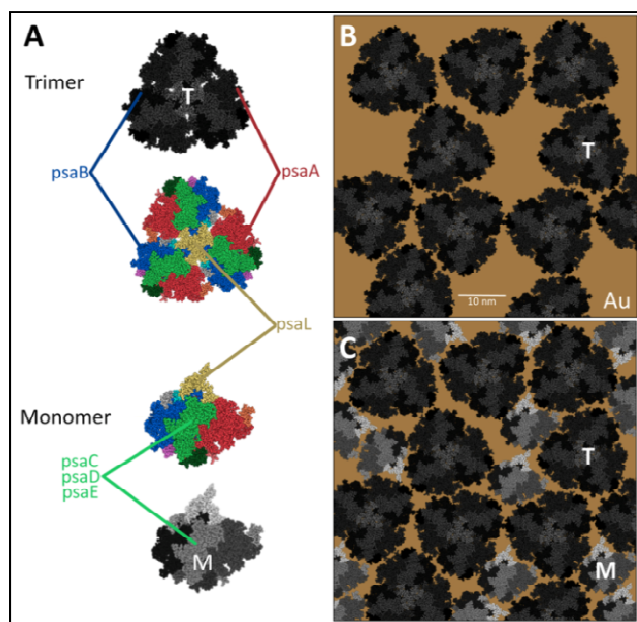


Figure 2. Improved surface coverage using electrodeposited trimers and monomers.

Figure 2 shows that a two-step deposition of monomer and trimer could yield an approximately 42% increase in surface coverage. To provide a uniform source of active, mature, and monomeric PSI particles, we plan to start with biochemically pure and uniform trimeric complexes and deconstruct them to their individual core monomers. However, the remarkable stability of this trimer makes this disruption difficult and may lead to partial denaturation or loss of core subunits. We have completed a study to explore various methods to dissociate the PSI trimer into monomers. These treatments include heating, freeze/thaw cycles, and detergents.

2.2 Abiotic Integration Approach, Materials, and Methods

2.2.1 Surface Assembly

While the use of PSI as a biomolecular reactor for hydrogen generation has been demonstrated previously by Iwuchukwu et al. (6), the direct use of this technology in the Army would be greatly limited by the solution nature of the system. Thus, it is imperative that the system be integrated in a surface assembled fashion in order to progress toward a solid-state device. However, significant challenges are introduced with the surface assembly of biologicals—especially transmembrane proteins, such as PSI—that possess large hydrophobic regions. Specifically, the protein must be stabilized on the surface; we have done so in this work by chemically modifying the substrate's surface. In this case, PSI must also be electronically coupled to the electrode in order to encourage efficient electron transfer. Finally, these nanoentities must be controllably assembled to optimize the conditions of the biohybrid surface.

In this series of studies, PSI was deposited onto gold electrodes, which act as a model surface. These surfaces are chemically modified using monolayers of alkanethiols with varying functional tail groups. PSI was adsorbed onto the substrate using electrophoretic deposition (EPD). EPD consisted of a two-electrode cell in a 1-cm cuvette; a platinum wire electrode acted as the counter electrode (CE) and reference electrode (RE), while the working electrode (WE) was the gold chip. A -2V potential was applied to the cell in order to deposit the PSI onto the WE. After deposition, the gold chips were rinsed thoroughly with deionized water and dried with nitrogen gas. Samples were stored in the dark at $6\text{ }^{\circ}\text{C}$. Atomic force microscopy (AFM) was employed to quantify the amount of PSI adsorbed onto the Au surface.

2.2.2 Electrochemical and Photoelectrochemical Approach

Cyclic voltammetry (CV) and alternating current voltammetry (ACV) were used to study the quality of Surface Assembled Monolayers (SAMs) assembly and to measure the electron transfer rate of the SAMs, respectively. Both tests were conducted in a three-electrode cell with a Pt wire CE, and an Ag/AgCl RE. The electrolyte in both tests was 0.25M KCl and 0.5 mM potassium ferricyanide.

A photoelectrochemical apparatus was designed and constructed to measure the photoactivity of constructed electrodes. The electrochemical cell is a typical apparatus for photoelectrochemical solar cell measurements, enabling a wide range of measurements of various WEs by manipulating the incident illumination, electrolyte concentrations, and applied potentials.

Measuring the photocurrent generated by electrodes correlates to the potential hydrogen production an electrode can sustain. Hydrogen generation rates are directly correlated to the amount of electrons provided by the photoactive material through equation 1.



Monolayers of PSI have produced photocurrents that are on an order of magnitude smaller than the minimal 7.5 nA/cm^2 target (7). By increasing the deposition film thickness, and therefore the protein deposition density, we can show that photocurrents increase several orders of magnitude (8). The steric limitations of this geometry, however, would limit the production of hydrogen gas. Rougher surfaces have been demonstrated to increase the photocurrent produced by PSI electrodes (9).

2.2.2.1 Mediators

Osmium-(2,2'-bipyridyl)-dichloride [$\text{Os}(\text{bpy})_2\text{Cl}_2$] was used as an abiotic electron donor and methyl viologen (MV^{2+}) was used as an electron acceptor to harvest electrons from the PSI's stromal hump. These redox mediators are both in lieu of using the natural proteins cyt c_6 and Fd to direct the electron transfer.

2.2.2.2 Polymers for PSI Immobilization/Assembly

Poly-vinylimidazole (PVI) and Nafion were also employed to assemble/entrap PSI and $\text{Os}(\text{bpy})_2\text{Cl}_2$. Polymers are a simple method to construct PSI electrodes with more than a monolayer coverage. By entrapping $\text{Os}(\text{bpy})_2\text{Cl}_2$ in the polymer matrix the films become conductive, which provides for high-surface densities of PSI. The Nafion matrix was chosen because it allows for positive charges to diffuse through aqueous pores, but retains negative or uncharged species. This allowed for significant retention of PSI protein and $\text{Os}(\text{bpy})_2\text{Cl}_2$ to increase lifetimes while allowing the redox mediator MV^{2+} to collect photoelectrons from PSI. The polymer films were also deposited onto Au coated ITO glass electrodes.

2.3 Multiscale Modeling Approach

A variety of modeling approaches were used to best address the diversity of experimental phenomenon under study and to compare to relevant phenomenological trends. Electrostatic and structural analysis were used to assess the possible binding orientation of the protein complex on multiple surfaces, to propose suitable SAM composition for PSI surface binding, and to assess possible interactions between the PSI complex and substrate—such as the $\text{Os}(\text{bpy})_2$ moiety of the redox polymer. The structure of the PSI – cyt c_6 complex has not been determined experimentally. Therefore, advanced docking techniques were used to predict the complex structure and binding mode, to assess binding mode and electron transfer path in a variety of complexes using engineered cyt c_6 , and to propose alternative linkers for cyt c_6 oligomers.

2.3.1 PSI Surface Interactions and Environmental Effects

Structural studies are based upon the 1JB0 crystal structure of Jordan et al. (5) and use the Visual Molecular Dynamics (VMD) visualization software of Schulten et al. (10). Protonation patterns and pH effects are studied using the H++ pK prediction server of Virginia Tech (11).

2.3.2 PSI – cyt c_6 Complex Structure and Interactions

The structure of the docked PSI-cyt c_6 complex was studied using the Rosetta Docking Suite (12) and the ARL XPairIt (13) docking protocol. The structure of the PSI-plastocyanin complex was also determined for validation against experimentally derived structures. RosettaDesign was used for the design of putative improved linker (14).

2.3.3 Molecular Dynamics Approaches

The size of PSI (>24,000 non-hydrogen atoms) and the need for a highly accurate structural model led us to use all-atom molecular dynamics (MD) as an initial approach to model static bond and atom interactions. Following discussions within the group we developed a model based on the cyanobacterial x-ray structure published by Jordan et al. (5) (Protein Data Bank [PDB] ID: 1JB0) that included all ligands in the model published with the exception of the single calcium ion. Molecular dynamics and self-guided Langevin dynamics (SGLD) were performed on this model using the Assisted Model Building with Energy Refinement (AMBER) modeling suite.

2.3.4 Force Field Parameterization

For many of our molecules, we were able to take force field atom types and terms directly from the general AMBER force field. Restrained electrostatic potential (RESP) atomic charges for α -chlorophyll A; β -carotene; PQN; 1,2-dipalmitoyl-phosphatidyl-glycerole; 1,2-distearoyl-monogalactosyl-diglyceride; and the 1,11-bis(maleimido)triethylene glycol (BM(PEG)3) linker were calculated consistent with the AMBER ff99SBildn force field, as described by Lindorff-Larsen et al. (15). This process was simplified and partially automated using the RESP ESP charge Derive software toolkit developed by Francois-Yves Dupradeau (16).

In addition to the molecules just described, RESP atomic charges were calculated for both the reduced and oxidized form of iron sulfur clusters found in PSI. A deviation in the approach for calculating atomic charges was necessary because of known and well-documented limitations in Hartree-Fock representations of heavy metals. We modified the attached ligand representation to use complete amino and carboxy-terminal capped dipeptides and reparameterized. Results with these improved parameters are shown in following section.

Due to the size of the PSI complex, coarse-grained potentials of the MARTINI variety were of interest to facilitate long-time dynamics of the monomer, as well as to enable simulation of the PSI trimer. This required development of coarse-grained potentials—particularly for ligands involved in electron transfer—such as phyloquinone.

2.3.5 Quantum Mechanics

Quantum mechanical analysis has been performed on components of the PSI to understand the electronic landscape of the system, and to benchmark against other computational studies. In particular, the P700 active site of the PSI complex has been previously studied computationally. However, the current work is the first such study to analyze a thermally relaxed P700 complex from extended dynamic simulation, and as such provides an interesting basis for comparison. For the P700 models, quantum calculations were performed at the B3LYP/6-31G(d,p) level using the Gaussian software suite g09. Time dependent density functional theory (TDDFT) was performed on these models using the GAMESS code (17).

The Os(bpy)₂ moiety of the redox polymer used in the Abiotic Integration portion of this project is also of quantum mechanical interest, from the perspective of electron transfer energetics and also for the analysis of electrostatic mapping, which may help pinpoint how this complex prefers to orient itself relative to the luminal surface of the PSI complex (particularly near the P700 site). Variants of this complex (with varying types of ligands, varying numbers of ligands, and varying charge and spin state) were studied at the B3LYP/LANL2DZ level using the Gaussian software suite. The charge polarization density of both the Os(bpy)₂ complex and the beta barrels directly contiguous to the P700 site were mapped with the COSMOtherm package.

3. Results

3.1 Biochemical Approach

3.1.1 Conversion of the PSI Trimer Into a Functional Monomer

The PSI monomer from *T.e.* was isolated from native PSI trimers via a freeze-thaw treatment in the presence of the surfactant octylthioglucoside (OTG). This freeze-thaw treatment caused the trimer complex to dissociate into its individual monomers, whereby the newly exposed hydrophobic surfaces of the protein were passivated by OTG to prevent reassociation. Figure 3 depicts how the concentration of OTG in the freeze-thaw process dictates the monomeric yield. At a concentration of 3.75 mg/mL OTG the resulting PSI is nearly all monomer with only a trace of trimer left. After purifying by extracting bands from the sucrose gradient a BN-PAGE (figure 3c) showed that the isolated PSI was pure of other oligomeric states. A dimer was observed to also form during the treatment, especially in intermediate OTG concentrations, but was dissociated into monomers at 3.75 mg/mL OTG. Figure 3d shows STEM images of dispersed purified PSI monomer and trimer. It is seen that circular trimeric oligomers are lost once the monomerization process is completed. The resulting monomeric units were oblong in shape with a narrow width of approximately 10 nm, and a length of approximately 16 nm; whereas the trimer groups were circular in shape with a diameter of approximately 22 nm.

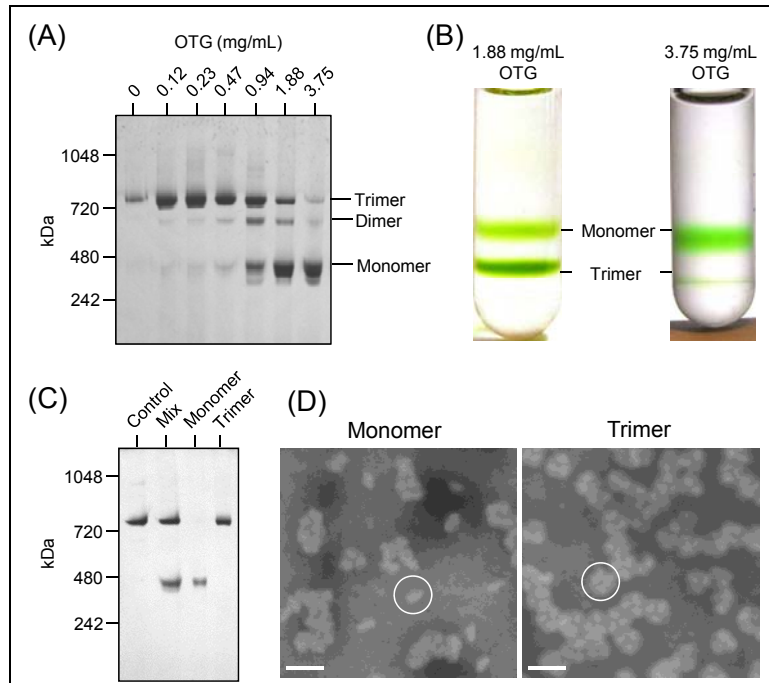


Figure 3. PSI monomer preparation from PSI trimer.
 (a) BN-PAGE of freeze-thaw treated PSI trimer with different concentration of detergent OTG.
 (b) Separation of PSI trimer from monomer using sucrose density gradient ultracentrifugation demonstrating the different yields using 1.88 mg/mL and 3.75 mg/mL OTG.
 (c) BN-PAGE of isolated PSI monomer and trimer. Control and mix represents untreated and treated PSI trimer using 1.88 mg/mL OTG. Monomer and trimer bands are after separation of the mixture with OTG.
 (d) STEM images of PSI monomer and trimer. Scale bar is 30 nm, with examples of individual monomers and trimers circled.

Using transient absorption spectroscopy it was seen that energy transfer between joined monomeric subunits does lead to more efficient photo-oxidation in the trimer versus the monomer. As shown in figure 4a, the optical signature of P700 photo-oxidation (ΔA_{705}) is greater for the trimer than the monomer at short flash durations, with equal chlorophyll-a concentrations. When ΔA_{705} was plotted against the log value of the incident photon flux (figure 4b), a sigmoidal relationship arises. A fit to one site-specific binding was calculated relating to the cooperation between the adjacent monomers. This analysis uses a fit from all three exposure times (5, 10, and 15 msec) for both the monomer and the trimer. This experiment allows direct comparison of the effective optical cross section of the two different oligomeric forms of PSI. This calculation was similar to what has been observed between cooperative allosteric enzymes, and can be reported as a Hill coefficient. The monomer's Hill coefficient is near 1 (1.08 ± 0.044) and indicated very little energy transfer or antenna coupling in monomeric PSI. However, the native trimeric form of PSI displays significant cooperativity ($h = 1.4 \pm 0.097$). This implies that under continuous illumination individual P700 sites turned over markedly more in the trimer than in the monomer.

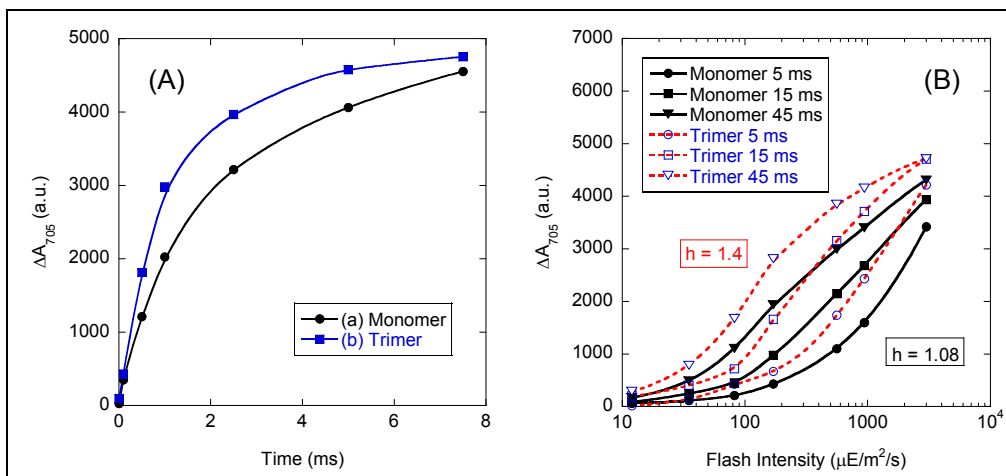


Figure 4. Transient absorption of monomer and trimer PSI with various flash times (a) and different flash intensities (b). The monomer and trimer were fit to determine the Hill coefficients.

To investigate how poly-vinylimidazole electrodes of PSI monomer and trimer respond to various light levels the incident power was varied between $0.25 \text{ mW}/\text{cm}^2$ and $2.5 \text{ mW}/\text{cm}^2$, as shown in figure 5. Below an incident power of $1 \text{ mW}/\text{cm}^2$ both systems showed an essentially linear response to an increase of light power, while also demonstrating similar photocurrents with the trimer slightly outpacing the monomer. Also, both samples showed a roll off with incident powers above $1 \text{ mW}/\text{cm}^2$, indicating that chlorophyll within PSI was becoming saturated. Interestingly, as the power was increased to intensities consistent with the AM 1.5 solar spectrum ($2.28 \text{ mW}/\text{cm}^2$ at 676nm) the trimer electrodes produced 20%–50% more photocurrent than monomer samples. The saturation of the monomer's photocurrent showed a leveling off at $2 \text{ mW}/\text{cm}^2$, whereas the trimer still showed a slight increase in photocurrent with intensity indicating it was not fully saturated at that level.

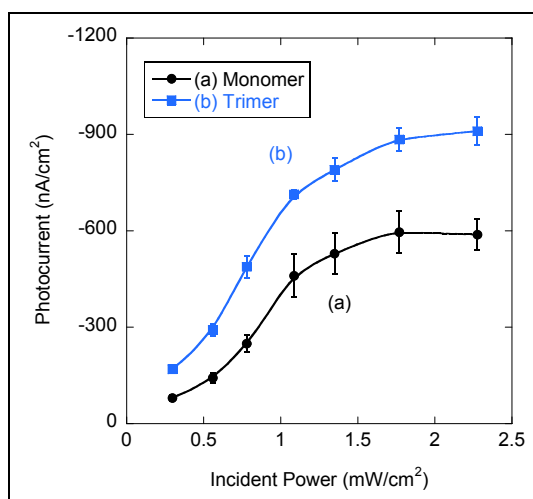


Figure 5. Photocurrent response of monomer (a) and trimer (b) electrodes at various incident light powers, wavelength 676 nm.

The trimer's greater activity at high-incident powers was attributed to extra chlorophyll-a molecules contained between monomers in the trimer complex, which are missing in the monomer system contributing to the trimer's greater maximum absorbing ability per PSI. The extra chlorophylls are also likely the origin of the energy transfer observed in figure 4. To confirm that trimer contains more chlorophyll-a than monomeric PSI, the protein concentration of the monomer and trimer PSI solutions (with equal chlorophyll-a concentration) was measured using a Bradford protein assay. Monomerized PSI, with a chlorophyll-a concentration of 0.115 mg/mL Chl, was found to have a protein concentration of 0.22 mg/mL PSI whereas the trimer (0.112 mg/mL Chl) was 0.18 mg/mL PSI, thus yielding a ratio of 0.509 mg_{Chl}/mg_{PSI} for monomer and 0.639 mg_{Chl}/mg_{PSI} for the trimer. Therefore, trimeric PSI contained 25% more chlorophyll-a than the isolated monomers, which corresponds well with the range of a 20%–50% increase in photocurrent of trimer over monomeric electrodes at high-incident powers, shown in figure 5. The difference in photocurrent may occur predominately at higher incident powers because the two forms were able to absorb light and produce photoelectrons with equal efficiencies at lower powers.

3.2 Abiotic Integration Approach (Electrochemistry and Photoelectrochemistry)

3.2.1 PSI Surface Assembly

This work demonstrates the improved assembly of PSI via electrophoretic deposition, with controllable surface assembled PSI density, on different self-assembled alkanethiol monolayers. Using artificial electron donors and acceptors ($\text{Os}(\text{bpy})_2\text{Cl}_2$ and MV^{2+}) we demonstrated photocurrent generation from a single PSI layer. Photoelectrochemical comparison of the biohybrid systems assembled from different alkanethiols (hexanethiol, aminohexanethiol, mercaptohexanol, and mercaptohexanoic acid) reveals that the PSI-generated photocurrent is enhanced by almost five times on negatively charged SAM surfaces as compared to positively charged surfaces.

The information summarized in figure 6 demonstrates the effective and controllable assembly of active single layers of PSI on electrode surfaces. The deposition of PSI was prepared via electrophoretic deposition, where PSI binding was increased by almost three-fold on unfunctionalized Au surfaces, as compared to assembly via adsorption. The assembly of PSI on four SAMs (HT, AHT, MHO, and MHA) was also demonstrated, as shown in figure 6. PSI assembled in high density to the uncharged or negatively charged hydrophilic surfaces (MHO, MHA) and in slightly lower amount to the positively charged surface (AHT). PSI binding was negligible on the hydrophobic HT surface.

The generation of photocurrent in PSI single-layer films was also demonstrated, where the use of the redox molecule $\text{Os}(\text{bpy})_2\text{Cl}_2$ was essential to the transfer of electrons from the electrode to the P700 site in PSI. This was shown in short timeframes as well as operation for hours at a time in figure 6. Similarly, the redox mediator MV^{2+} was vital in the removal of photogenerated electrons from the terminal FB site. Photocurrent magnitude corresponded with PSI quantity in

the case of the MHO and MHA surfaces, but showed significantly reduced turnover rates in the AHT system (4.5 and 5 electrons/s per PSI in MHO and MHA, versus 1.2 electron/s per PSI in AHT). This implies that photocurrent magnitude was not driven solely by the amount of PSI on the surface, but also by the underlying surface composition. Finally, the longevity of this active biofilm was demonstrated, where PSI monolayers were stable and active for at least three hours of illumination. Photocurrent magnitude increased over time for both the MHO and MHA electrodes, likely due to the increased amount of $\text{Os}(\text{bpy})_2\text{Cl}_2$ molecules that were able to diffuse to PSI over time. Combined, these results demonstrate the effect of surface composition on PSI assembly and photoactivity.

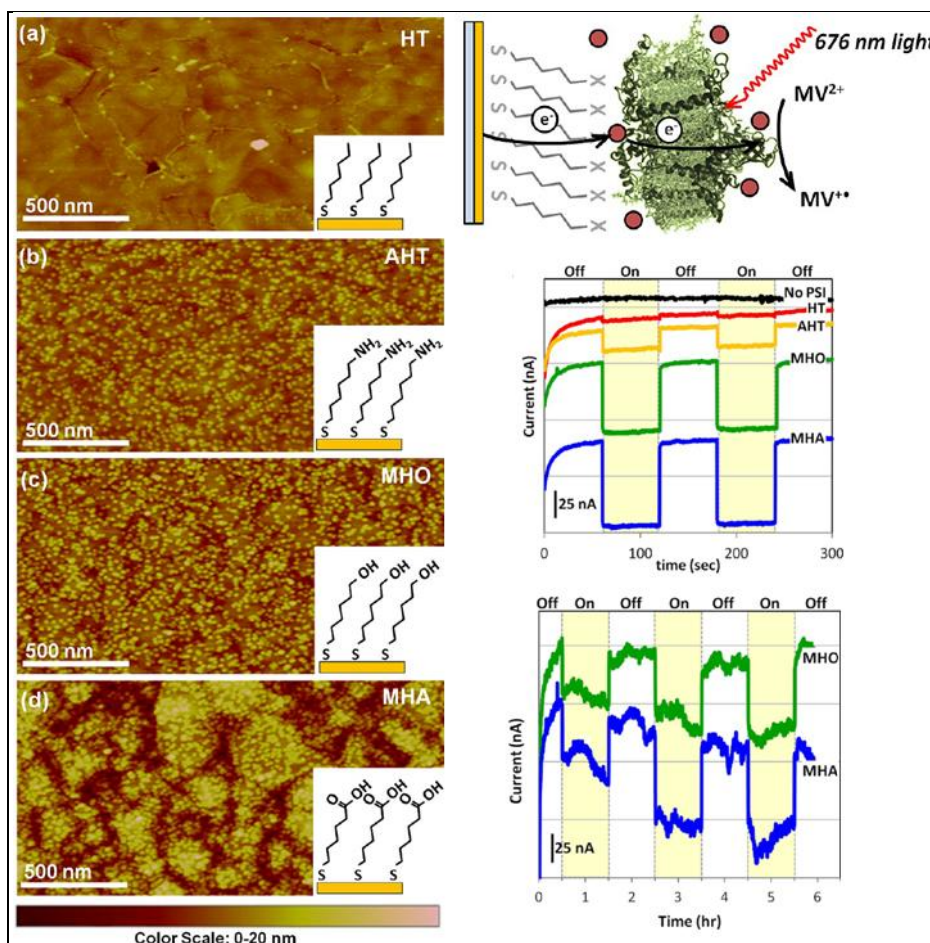


Figure 6. Summation of the results from immobilization of PSI on self-assembled monolayers of modified alkane thiols on gold substrates (18).

3.2.2 Polymer Hosts and Encapsulation

3.2.2.1 Poly-Vinylimidazole

The surface coverage of PSI on SAM functionalized electrodes is the limiting factor for photocurrent magnitudes. Any deposition beyond a complete monolayer leaves PSI unconnected to the electrode and can have a detrimental effect on cell performance. A conductive polymer

composed of a PVI backbone with $\text{Os}(\text{bpy})_2\text{Cl}_2$ redox centers present in the matrix was used to encapsulate PSI. This polymer was first developed by the Bardura group and had demonstrated high photocurrents up to $20\mu\text{A}/\text{cm}^2$ thanks to the elimination of the monolayer limit. This substrate was used to investigate the differences between monomeric and trimeric forms of PSI. Plants and higher order species typically contain PSI in a monomeric state whereas cyanobacteria typically use PSI which arranges as a trimer. Many groups use either trimer or monomer without regard to any structural differences the arrangement may provide. The PVI polymer was used to investigate the differences between the two structures of PSI as part of the monomer study described in the Biochemistry sections.

When compared on an equal chlorophyll basis trimer and monomer electrodes were found to perform similarly. In figure 7 it was seen that the similarities between monomeric and trimeric PSI cover the entire visible spectrum and that the photocurrent resulting from the cell reflects the absorption spectrum of PSI. The photoaction spectrum in figure 7B shows that the $\text{Os}(\text{bpy})_2\text{Cl}_2$ in the PVI film does not contribute any photocurrent to the system despite its absorbance in the blue region of the spectrum.

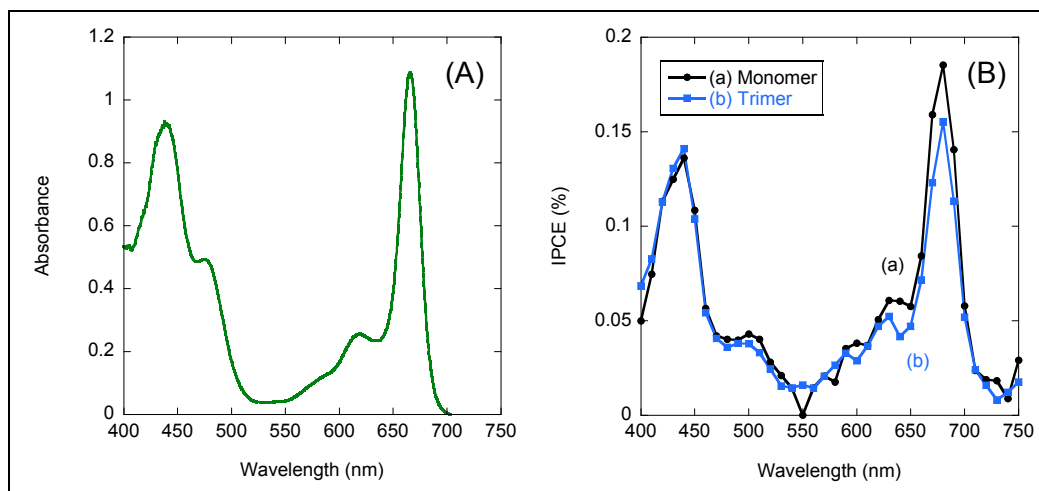


Figure 7. Absorbance spectrum (A) of PSI trimer solution. IPCE photoaction spectra (B) of PSI monomer (a) and trimer (b).

3.2.2.2 Nafion

The PVI backbone is good for attaching $\text{Os}(\text{bpy})_2\text{Cl}_2$, but it was found that loose $\text{Os}(\text{bpy})_2\text{Cl}_2$ is more essential to the cell's activity. Loose $\text{Os}(\text{bpy})_2\text{Cl}_2$ was found to leak out of the PVI film easily, which resulted in a significant reduction of activity of the electrode over time. To alleviate leaching, polymer films were made with Nafion, which prevents species from diffusing if they are not positively charged. PSI and $\text{Os}(\text{bpy})_2\text{Cl}_2$ were mixed into the polymer as described above. Because of the higher retention, PSI could be loaded at much higher concentrations into the film than in the previous PVI samples increasing electrode photocurrents. Figure 8 shows the optimization of PSI concentrations whereby it was found high concentrations of PSI can block

the lower layers that are more connected to the support electrode. The Nafion surface density was also optimized because too much Nafion prevented electron scavenging mediators from diffusing through the film and too little Nafion caused the film to lose $\text{Os}(\text{bpy})_2\text{Cl}_2$.

Polymer films have shown their ability to increase photocurrent beyond what SAM architectures can produce by building a three-dimensional (3-D) film that isn't limited to the electrode's surface area. There is still more room to improve as each PSI reaction center should be able to process 1000 electrons per second. Future work aims to address improving the kinetics of the photohole scavenging species $\text{Os}(\text{bpy})_2\text{Cl}_2$.

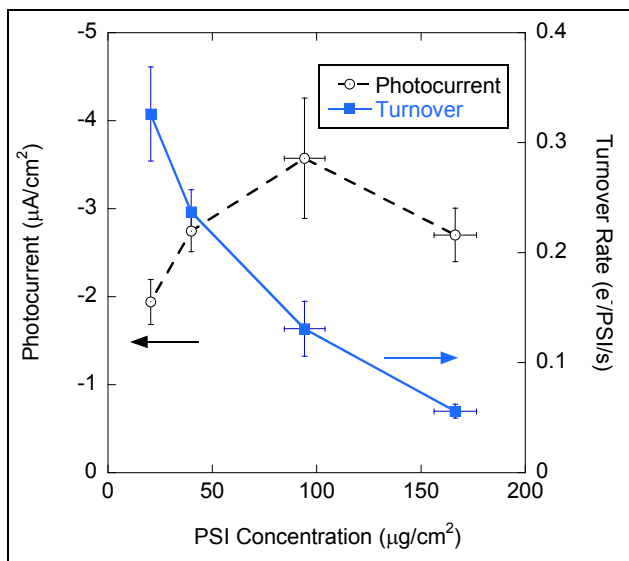


Figure 8. Optimization of PSI in the Nafion films. The current output reaches a maximum at $100\mu\text{g}/\text{cm}^2$. The turnover rate shows that the current from an individual protein is reduced due to blocking effects from upper layers.

3.2.3 Pt Catalysts

The two methods to incorporate Pt with PSI found in literature are by (1) photoreducing H_2PtCl_6 which forms uncapped Pt nanoparticles on the PSI proteins and (2) attaching presynthesized Pt nanoparticles to PSI either through adsorption or with a molecular tether. The photoreduction mechanism was employed previously by Iwakumu et al. (6) and was successful for reducing water to produce H_2 gas at low levels. The presynthesis route has been the method that has produced the highest rates of hydrogen production. Therefore, platinum nanoparticles were synthesized to incorporate them with PSI using a postsynthesis method.

Figure 9 shows Pt nanoparticles formed by reducing H_2PtCl_6 with NaBH_4 and capped with a hydrophilic agent mercaptohexanoic acid. The capping agent was used to prevent aggregation of Pt nanoparticles. Nanoparticles were attached to PSI by mixing a PSI solution with a Pt nanoparticle solution and tumbling. The resulting product was filtered and deposited onto Au/ITO electrodes for photoelectrochemical characterization similar to the functionalized

surfaces described in previous sections. Small photocurrents were detected (approximately $5\text{nA}/\text{cm}^2$) with no MV^{2+} in solution implying that the PSI-Pt complex was capable of performing photocatalytic reactions. The amount of photocurrent was too small to detect if the resulting reaction products were H_2 gas or some other reduction species. The photocurrent was not present when no Pt was incorporated with PSI indicating that Pt catalyst particles are needed to provide a reduction pathway.

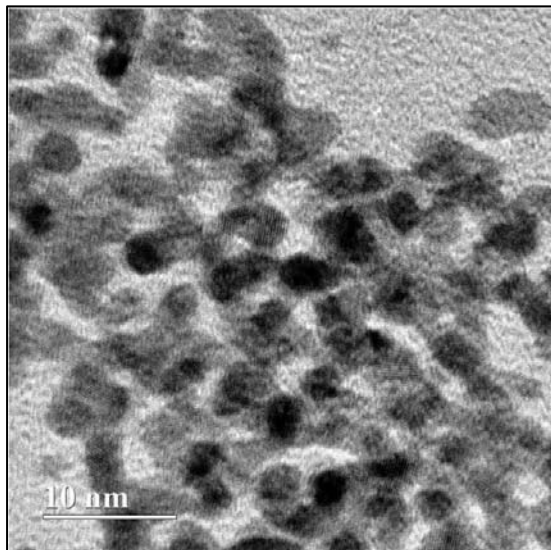


Figure 9. Pt nanoparticles capped with mercaptohexanoic acid. The nanoparticles were dropcast onto the TEM grid and air dried. Reduction was performed by NaBH_4 . The scale bar is 10 nm.

The low levels of photocurrent could be attributed to the electrochemical potential of the $\text{Os}^{3+}/\text{Os}^{2+}$ hole scavenging species $\text{Os}(\text{bpy})_2\text{Cl}_2$, which is too negative to perform the water oxidation reaction. H_2O_2 was introduced as a trace species because its reduction potential is more negative than $\text{H}_2\text{O}/\text{O}_2$. When the PSI-Pt complexes were illuminated in the presence of H_2O_2 the photocurrent was seen to jump to approximately $200\text{nA}/\text{cm}^2$ indicating that catalytic photoelectrons are available at the Pt nanoparticles and that the system can function as long as a sacrificial species is electrochemically available to oxidize. This is exactly why all previous systems have used ascorbic acid as a sacrificial electron donor to PSI, and why nature uses both PSI and PSII in tandem to split water.

3.3 Multiscale Modeling Results

3.3.1 PSI Surface Interactions and Environmental Effects

Structural analysis of the protein complex is useful on many levels and can be used to approach the question of how best to bind the PSI complex to an electrode surface (e.g., Au or monolayer-covered Au) in a controlled and predictable orientation. For instance, the sulfur moiety of the amino acid cysteine has long been recognized as providing a strong, direct linkage for

immobilizing a protein on a gold surface. In the case of PSI, this would require modifications to the protein sequence, as a quick analysis demonstrates that wild-type PSI has no readily accessible cysteine residues to bind to Au.

Alternatively, for an Au surface covered with a SAM consisting of carboxylic acid-terminated amphiphilic molecules, one would expect interaction with the positive hydrophilic amino acids lysine, arginine, and histidine on the protein moiety. However, these residues are found in abundance on both luminal and stromal faces of the PSI complex, and therefore do not provide a key to proper orientation.

This then raises the question of the benefits of orienting the PSI complex through choice of SAM. The PSI complex was analyzed by applying the Kyte-Doolittle and Eisenberg scales, which provide quantization of the relative hydrophobicity of the amino acid residues within the complex. The surface was also mapped by residue type (figure 10). It is not surprising to note that the luminal surface is largely hydrophilic, as this is an integral membrane protein complex and this surface tends to be exposed, as shown in the schematic in figure 1. This corroborates the poor results of the hydrophobic HT SAM shown *experimentally* in figure 6. Mapping by residue type shows a preponderance of polar (green) residues at the luminal surface, residues that are chemically reasonable to demonstrate a strong interaction with uncharged or negatively charged hydrophilic functional groups—such as the MHO and MHA, also shown *experimentally* in figure 6.

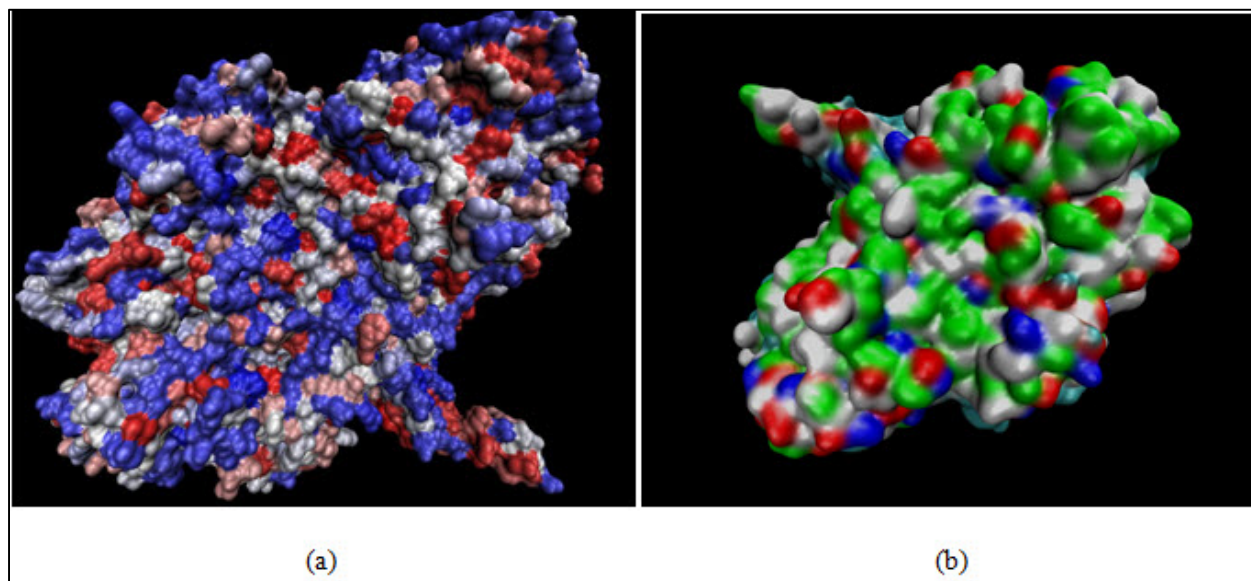


Figure 10. (a) Representation of the hydrophobicity (blue represents hydrophilic, red represents hydrophobic); and (b) residue character (red represents acidic, blue represents basic, white represents nonpolar, and green represents polar residues) of the PSI luminal surface.

In the course of this project, questions were raised on the possible effect of pH on binding to the electrode surface, as well as on the electron transfer chain. A mapping of pH effects in PSI at pH

of 5.5, 6.5, and 7 is of interest because some residues—notably histidine—are sensitive within that range. A mapping of affected residues demonstrates a cluster of affected residues on the luminal surface a short distance away from the P700 entry site, with possible effects on attachment. Several residues in the vicinity of the stromal Fe-S sites also appear to be affected. There may be implications for electron transfer, a topic for future work.

3.3.2 PSI – cyt c_6 Complex Structure

Rigid docking with the Rosetta docking suite was performed on the PSI-plastocyanin complex as a validation of the method, and compared to experimental data. These were ranked by energy and distance between the plastocyanin copper atom and PSI P700 magnesium atoms, and the five most favorable structures analyzed. Of these five structures, all share an identical (correct) docking face, and three closely resemble the published result.

Results of docking of cyt c_6 with PSI are cloudier. Ranking by energy and distance between cyt c_6 heme iron and P700 magnesium shows no common binding orientation or contact face. This failure may be in part due to conformational changes upon binding that were not captured in this protocol, poor representation of electrostatics, or poor parameterization in general. We do note that the docked complexes demonstrate rotation of the cyt c_6 to allow interaction of the heme cleft with the luminal surface, in agreement with previous work.

The consensus orientation result from this docking study was then used to design cyt c_6 oligomers in collaboration with the experimental oligomer studies of the University of Tennessee-Knoxville and ARL. The designed linkerless cyt c_6 oligomer is predicted to have a greatly reduced distance between heme iron atoms compared to previously tested oligomers (table 1). Experimental tests of this system are currently underway.

Table 1. Predicted distance (Angstroms) between heme iron atoms.

1C6S-fusion dimer	34.522
1C6S-Ala-dimer	38.419
1C6S-Ser-dimer	47.401
1C6S-TruncatedFusion-dimer	31.181
1C6S-TruncatedTail-dimer	34.296
1C6S-Designed	22.800

3.3.3 Molecular Dynamics

Iron-sulfur centers are vital to the electron-transfer chain of PSI, as well as to a variety of other metalloproteins involved in generation of radicals, regulation of gene expression, and oxidative phosphorylation.

The state of the practice in generation of atomic charges for forcefield development led to overly polarized charges, which disrupted the structure (figure 11a, note how the stromal hump of the silver (molecular dynamics) structure is starting to unfold away from the known crystal structure

(red). This is also evident in the RMSD (root mean square displacement, figure 11b), which shows differences between the MD structure and the crystal structure continuing to grow during the course of the simulation.

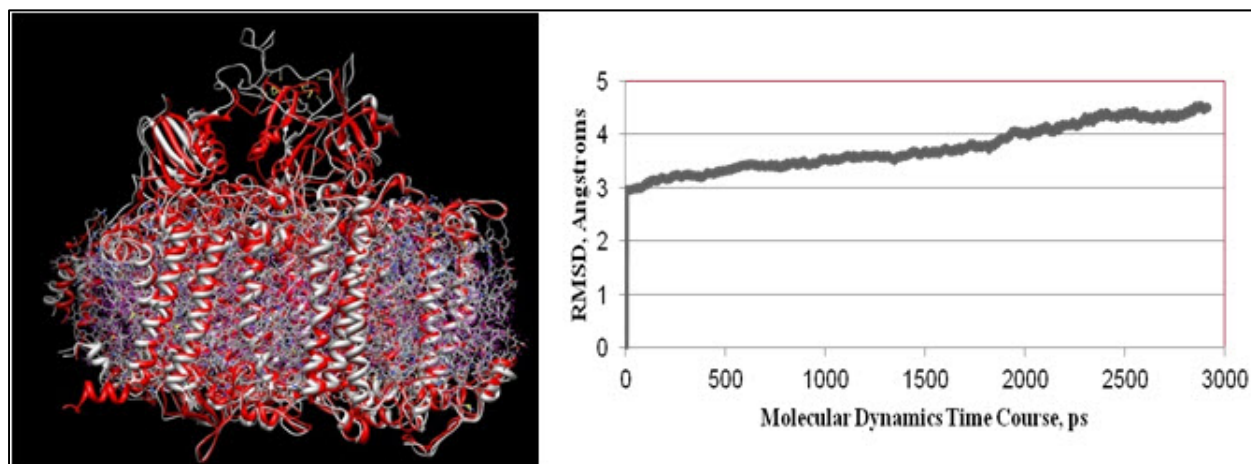


Figure 11. (Left) Relaxed structure (silver) of the PSI complex after molecular dynamics, compared to the original crystal structure (red). (Right) the unfolding in the stromal hump is seen in the growth of Root Mean Square Deviation (RMSD) from the crystal structure coordinates during the course of the simulation (20).

With our improved charges (figure 12) the entire structure (tan) is stable relative to the crystal structure (red) and stays stable (RMSD plot) during the course of this simulation. This is the longest known molecular dynamics simulation of this very large system.

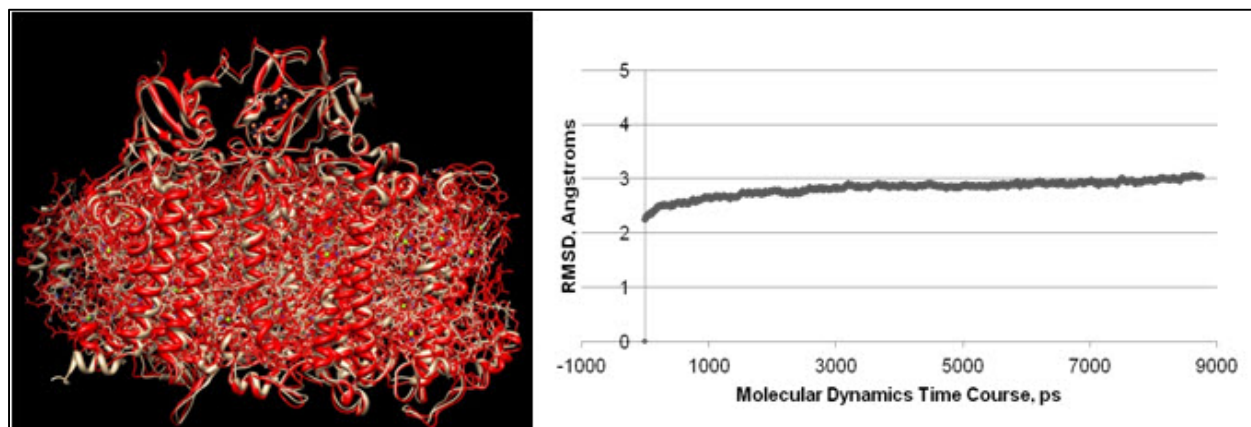


Figure 12. Molecular dynamics simulation with the improved iron-sulfur center parameters showing greatly improved stability (20).

A relaxed, dynamically thermalized structure may then be used to analyze possible fluctuations in distances along the electron transfer chain (ETC) of this system. We also note possible difference between the A and B branch of the ETC, as dominance of one branch over the other is still debated within the literature. These distances are tabulated below and compared to the original crystal structure.

Table 2. Measured distances between electron carriers in the PSI x-ray and initial MD structures (20).

Measured Distance	X-Ray Structure	MD Model
P700 chlorophylls	6.34 Å	5.80 Å
P700A to A-1A	11.72 Å	12.74 Å
A-1A to A0A	8.13 Å	8.74 Å
A0A to A1A	8.78 Å	9.89 Å
P700B to A-1B	11.95 Å	12.62 Å
A-1B to A0B	8.22 Å	7.60 Å
A0B to A1B	8.78 Å	9.37 Å
P700B to A1A	26.0 Å	26.2 Å

We note with interest that in general, thermal relaxation has increased distances within branch A of the model (compared to the original crystal structure) while distances within branch B have decreased. The net result is that, while distances within the original structure are similar between the A and B branches, there are marked differences between these distances in the thermalized structure, corroborating experimental differences seen in electron transfer rates.

Coarse-grained (MARTINI) parameters were developed for a variety of ligands in this complex, including β -carotene and phylloquinone, and validated in a series of lipid-bilayer simulations, compared to simulation of the associated all-atom model. An open-literature publication is planned.

3.3.4 Quantum Mechanics

Optimization of the $\text{Os}(\text{bpy})_2\text{Cl}_2$ parent and its derivative cation $[\text{Os}(\text{bpy})_2]^{2+}$ show an energetic preference for placing one bpy ligand along the equatorial axis of the central transition metal, and placing the other perpendicular to the first so that it binds in one axial and one equatorial location. A modified “square” interface with both bpy ligands bound along the central Os equatorial axis is also possible, and in this instance it is seen that one ligand will shift slightly out of the equatorial plan, but still leave sufficient room for the approach of an additional ligand. For purposes of binding to the redox polymer, the polymer sidechain attaching to the $\text{Os}(\text{bpy})_2$ complex is modeled as an imidazole. COSMO and electrostatic potential analysis of this structure shows a highly negatively charged spot representing freely available electrons around the central Os. A similar analysis (COSMO and electrostatic potential) of a model of the β -barrel loops directly adjacent to the P700 binding site show some SER residues near the center of the loops, which represent a reasonable first guess at a docking location on the PSI side. A more detailed energetic evaluation is underway.

Finally, we perform quantum-mechanical analysis of the PSI P700 site, the first work to do so on a classically thermalized structure. This is compared to analysis of the original crystal structure,

and the QM/MM optimized structure of Canfield et al. (19). The most striking structural difference between our thermalized P700 site and the other two structures is a reversion of the central magnesium atoms back into the plane of the chlorin ring. The way this manifests itself quantum mechanically is shown below in table 3.

Table 3. Physical and electronic structure properties of three P700 models at B3LYP/6-31G (d, p) (20).

	Current Work	1JB0	Canfield
IP (eV)	6.01	5.78	5.78
Frontier Orbital Energy HOMO (eV)	5.11	4.88	-4.89
Frontier Orbital Energy LUMO (eV)	2.91	2.57	-2.70
HOMO-LUMO eV	2.19	2.31	2.19
Mg-Mg Distance (angstroms)	5.80	6.30	6.26
HisN-Mg Distance (angstroms)	3.99/4.49	2.36/2.26	2.20/2.22
Heavy-Atom RMSD wrt 1JB0 (angstroms)	0.60	0.00	0.29

We note that, the energies of the frontier orbitals (highest occupied molecular orbital, or HOMO and lowest unoccupied molecular orbital, or LUMO) are different from the 1JB0 and Canfield models due to a change in Mg complexation pattern. The HOMO-LUMO gap for our model is approximately 0.1 eV smaller than in the experimental structure.

4. Conclusions

In this work we have demonstrated the ability to extract bacterial PSI and generate photocurrents in multiple different *ex vivo* environments. This includes operation of monolayers, multilayers on electrodeposited PVI films, and entrapped in 3-D Nafion films. It is possible to utilize natural, modified-natural, and completely synthetic electron donors and acceptors with PSI. There are indications that hydrogen generation from platinized PSI is possible but high-yield, highly efficient production of hydrogen in this fashion will take significantly more work.

We have also shown the capability to modify PSI from the native-trimer complex into individual monomeric units. This was successfully accomplished using a freeze-thaw treatment. Characterization of the resulting monomeric product showed that the monomer can be isolated to a high purity and stabilized with surfactants. The monomer was incorporated onto electrode surfaces and the photoactivity was compared to native-trimeric PSI showing little difference, which indicates that the monomer did not lose significant activity during the freeze-thaw treatment.

We have also demonstrated that a variety of modeling methods are needed to address the range of phenomenon studied, and have developed all of the necessary models and parameters. A set of parameters have been developed for the iron-sulfur centers of the PSI complex, which we expect to prove useful for a variety of proteins. These parameters were then used to perform the longest to-date classical dynamics simulation of this large system. This relaxed structure was then analyzed and the variation in distances between the electron carriers in the A and B channels of the complex were shown, providing a possible rationale for differences in electron transfer rates seen experimentally. Analysis of the PSI structure and residue placement along the stromal and luminal surfaces was used to predict PSI affinity for various SAM surfaces, and help experimental trends. A putative structure was obtained for the PSI-cyt c_6 complex, and theoretical techniques were used to help design linkers for more efficient cyt c_6 oligomers.

To conclude, each area of the original proposal has been advanced significantly. Biochemical and bioengineering methods have been utilized to modify the PSI on the binding sites on the luminal (electron accepting) side, the stromal (electron donating) side, disassembly to functional monomers and oligometrization of the cytochrome electron donors. Assembly and characterization techniques have been improved dramatically for both photocurrents and surface analysis. There were also significant advances in modeling methods that not only describe *ex vivo* function but logical pathways to improve PSI/abiotic hybrid structure performance.

5. References

1. Rochaix, J. D. Regulation of Photosynthetic Electron Transport. *Bba-Bioenergetics* **2011**, *1807* (3), 375–383.
2. Kerfeld, C. A.; Krogmann, D. W. Photosynthetic Cytochromes c in Cyanobacteria, Algae, and Plants. *Annu Rev Plant Phys* **1998**, *49*, 397–425.
3. Santabarbara, S.; Kuprov, I.; Poluektov, O.; Casal, A.; Russell, C. A.; Purton, S.; Evans, M. C. W. Directionality of Electron-Transfer Reactions in Photosystem I of Prokaryotes: Universality of the Bidirectional Electron-Transfer Model. *J Phys Chem B* **2010**, *114* (46), 15,158–15,171.
4. Busch, A.; Hippler, M. The Structure and Function of Eukaryotic Photosystem I. *Bba-Bioenergetics* **2011**, *1807* (8), 864–877.
5. Jordan, P.; Fromme, P.; Witt, H. T.; Klukas, O.; Saenger, W.; Krauss, N. Three-Dimensional Structure of Cyanobacterial Photosystem I at 2.5 Angstrom Resolution. *Nature* **2001**, *411* (6840), 909–917.
6. Iwuchukwu, I. J.; Vaughn, M.; Myers, N.; O'Neill, H.; Frymier, P.; Bruce, B. D. Self-Organized Photosynthetic Nanoparticle for Cell-Free Hydrogen Production. *Nat. Nanotechnol.* **2010**, *5* (1), 73–79.
7. Ciobanu, M.; Kincaid, H. A.; Lo, V.; Dukes, A. D.; Jennings, G. K.; Cliffel, D. E. Electrochemistry and Photoelectrochemistry of Photosystem I Adsorbed on Hydroxyl-Terminated Monolayers. *J. Electroanal. Chem.* **2007**, *599* (1), 72–78.
8. Faulkner, C. J.; Lees, S.; Ciesielski, P. N.; Cliffel, D. E.; Jennings, G. K. Rapid Assembly of Photosystem I Monolayers on Gold Electrodes. *Langmuir* **2008**, *24* (16), 8409–8412.
9. Ciesielski, P. N.; Scott, A. M.; Faulkner, C. J.; Berron, B. J.; Cliffel, D. E.; Jennings, G. K. Functionalized Nanoporous Gold Leaf Electrode Films for the Immobilization of Photosystem I. *Acs Nano* **2008**, *2* (12), 2465–2472.
10. Humphrey, W.; Dalke, A.; Schulten, K. VMD: Visual Molecular Dynamics. *J Mol Graph Model* **1996**, *14* (1), 33–38.
11. Anandakrishnan, R.; Aguilar, B.; Onufriev, A. V. H++3.0: Automating pK Prediction and the Preparation of Biomolecular Structures for Atomistic Molecular Modeling and Simulations. *Nucleic Acids Res* **2012**, *40* (W1), W537–W541.
12. Lyskov, S.; Gray, J. J. The RosettaDock Server for Local Proteinprotein Docking. *Nucleic Acids Res* **2008**, *36*, W233–W238.

13. Sellers, M. S.; Hurley, M. M. XPairIt: A Software Toolkit for Smart Peptide Reagent Design. *Abstr Pap Am Chem S* **2012**, 243.
14. Liu, Y.; Kuhlman, B. RosettaDesign Server for Protein Design. *Nucleic Acids Res* **2006**, 34, W235–W238.
15. Lindorff-Larsen, K.; Piana, S.; Palmo, K.; Maragakis, P.; Klepeis, J. L.; Dror, R. O.; Shaw, D. E. Improved Side-Chain Torsion Potentials for the Amber ff99SB Protein Force Field. *Proteins* **2010**, 78 (8), 1950–1958.
16. Dupradeau, F. Y.; Pigache, A.; Zaffran, T.; Savineau, C.; Lelong, R.; Grivel, N.; Lelong, D.; Rosanski, W.; Cieplak, P. The R.ED. Tools: Advances in RESP and ESP Charge Derivation and Force Field Library Building. *Phys Chem Chem Phys* **2010**, 12 (28), 7821–7839.
17. Schmidt, M. W.; Baldrige, K. K.; Boatz, J. A.; Elbert, S. T.; Gordon, M. S.; Jensen, J. H.; Koseki, S.; Matsunaga, N.; Nguyen, K. A.; Su, S. J.; Windus, T. L.; Dupuis, M.; Montgomery, J. A. General Atomic and Molecular Electronic-Structure System. *J Comput Chem* **1993**, 14 (11), 1347–1363.
18. Manocchi, A. K.; Baker, D. R.; Pendley, S. S.; Nguyen, K.; Hurley, M. M.; Bruce, B. D.; Sumner, J. J.; Lundgren, C. A. Photocurrent Generation from Surface Assembled Photosystem I on Alkanethiol Modified Electrodes. *Langmuir* **2013**, 29 (7), 2412–2419.
19. Canfield, P.; Dahlbom, M. G.; Hush, N. S.; Reimers, J. R. Density-Functional Geometry Optimization of the 150 000-Atom Photosystem-I Trimer. *J Chem Phys* **2006**, 124 (2).
20. Pendley, S. S.; Manocchi, A. K.; Baker, D. R.; Sumner, J. J.; Lundgren, C. A.; Hurley, M. M. Applications of Molecular Modeling to Challenges in Clean Energy; Fitzgerald, G.; Govind, N. ACS Symposium Series; American Chemical Society: Washington, DC, 2013.

6. Transitions

Further bioelectrochemical research on PSI and genetically modified PSI will be transitioned to the H47 Alternative Routes to Fuel line. We will use genetically modified PsaF and the linked cyt c_6 's developed in the biochemical approach to confirm increased binding affinity, which should result in higher electron transfer rates.

Iron-sulfur centers are vital to the electron transfer chain of PSI, as well as to a variety of other metalloproteins involved in generation of radicals, regulation of gene expression, and oxidative phosphorylation. The modeling protocol and parameters developed for the PSI iron-sulfur centers (publication in process) are currently being used as part of a new-start Director's Research Initiative (collaboration with the Sensors and Electron Devices Directorate [SEDD] and Computational and Information Sciences Directorate [CISD]) "Computational Design of External and Internal Metabolic Modulators of Bacterial Output" for simulation of regulatory enzymes in Clostridia.

In-house docking protocol used in this project to study the PSI/CytC6 complex is currently in use in an ICB collaborative project with SEDD/Cal Tech, and is additionally being used by ARL researchers in a community-wide docking benchmark called "CAPRI" or the Critical Assessment of Prediction of Interactions (<http://www.ebi.ac.uk/msd-srv/capri/>).

The electrostatic matching techniques used to study PSI/SAM and PSI/inorganic complex binding were used in a 2013 innovation project on the prediction of the structure of energetic material cocrystals. This was presented at the Division level in November and a transition to mission funding is being explored.

INTENTIONALLY LEFT BLANK.

List of Symbols, Abbreviations, and Acronyms

3-D	three-dimensional
ACV	alternating current voltammetry
AFM	atomic force microscopy
AMBER	Assisted Model Building with Energy Refinement
ARL	U.S. Army Research Laboratory
CAPRI	Critical Assessment of Prediction of Interactions
CE	counter electrode
CISD	Computational and Information Sciences Directorate
CV	cyclic voltammetry
EPD	electrophoretic deposition
ETC	electron transfer chain
Fd	ferredoxin
HOMO	highest occupied molecular orbital
LUMO	lowest unoccupied molecular orbital
MD	molecular dynamics
OTG	octylthioglucoside
PC	plastocyanin
PDB	Protein Data Bank
PSI	Photo System I
PVI	poly-vinylimidazole
RE	reference electrode
RESP	restrained electrostatic potential
RMSD	Root Mean Square Deviation
SAM	Surface Assembled Monolayer

SEDD	Sensors and Electron Devices Directorate
SGLD	self-guided Langevin dynamics
TDDFT	time dependent density functional theory
<i>T.e.</i>	<i>Thermosynechococcus elongatus</i>
VMD	Visual Molecular Dynamics
WE	working electrode

NO. OF
COPIES ORGANIZATION

1 DEFENSE TECHNICAL
(PDF) INFORMATION CTR
DTIC OCA

2 DIRECTOR
(PDF) US ARMY RSRCH LAB
RDRL CIO LL
IMAL HRA MAIL & RECORDS MGMT

1 GOVT PRINTG OFC
(PDF) A MALHOTRA

1 US ARMY RSRCH LAB
(PDF) RDRL SED C
C LUNDGREN